Solar Phys
DOI 10.1007/s11207-015-0685-0

3D Reconstruction of Interplanetary Scintillation (IPS) Remote-Sensing Data: Global Solar Wind Boundaries for Driving 3D-MHD Models

H.-S. Yu[1] · B.V. Jackson[1] · P.P. Hick[1] · A. Buffington[1] · D. Odstrcil[2,3] · C.-C. Wu[4] · J.A. Davies[5] · M.M. Bisi[5] · M. Tokumaru[6]

Received: 17 December 2014 / Accepted: 10 April 2015

Abstract The University of California, San Diego, time-dependent analyses of the heliosphere provide three-dimensional (3D) reconstructions of solar wind velocities and densities from observations of interplanetary scintillation (IPS). Using data from the Solar-Terrestrial Environment Laboratory, Japan, these reconstructions provide a real-time prediction of the global solar-wind density and velocity throughout the whole heliosphere with a temporal cadence of about one day (ips.ucsd.edu). Updates to this modeling effort continue: in the

Radio Heliophysics: Science and Forecasting
Guest Editors: Mario M. Bisi, Bernard V. Jackson, and J. Americo Gonzalez-Esparza

✉ H.-S. Yu
hsyu@ucsd.edu

B.V. Jackson
bvjackson@ucsd.edu

P.P. Hick
pphick@ucsd.edu

A. Buffington
abuffington@ucsd.edu

D. Odstrcil
dusanod@gmail.com

C.-C. Wu
chin-chun.wu@nrl.navy.mil

J.A. Davies
jackie.davies@stfc.ac.uk

M.M. Bisi
mario.bisi@stfc.ac.uk

M. Tokumaru
tokumaru@stelab.nagoya-u.ac.jp

1 Center for Astrophysics and Space Sciences, University of California at San Diego, 9500 Gilman Drive #0424, La Jolla, CA 92093-0424, USA

2 George Mason University, 4400 University Drive, Fairfax, VA 22030, USA

3 NASA/GSFC M/C 674, Greenbelt, MD 20771, USA

Published online: 29 April 2015

present article, near-Sun results extracted from the time-dependent 3D reconstruction are used as inner boundary conditions to drive 3D-MHD models (*e.g.* ENLIL and H3D-MHD). This allows us to explore the differences between the IPS kinematic-model data-fitting procedure and current 3D-MHD modeling techniques. The differences in these techniques provide interesting insights into the physical principles governing the expulsion of coronal mass ejections (CMEs). Here we detail for the first time several specific CMEs and an induced shock that occurred in September 2011 that demonstrate some of the issues resulting from these analyses.

Keywords Interplanetary scintillation · Solar wind · 3D-MHD models · Remote sensing · Forecasting

1. Introduction

The solar wind is a stream of hot, strongly turbulent plasma, flowing outward in all directions from the Sun throughout the solar system at speeds of about 400 $\mathrm{km\,s^{-1}}$. On average, it takes around four days for an individual feature in the ambient solar wind to travel the ≈ 1 AU distance from the Sun to the Earth. Transient structures such as coronal mass ejections (CMEs) and their interplanetary counterparts (ICMEs/shocks), which evolve on short time scales (hours to days) are usually thousands of times larger than Earth, and the very fastest ones can reach Earth in less than one day. These short-duration interplanetary disturbances and CMEs are associated with geomagnetic storms (*e.g.* Gosling *et al.*, 1991). Understanding the fundamental physical processes of these near-Earth space-environment variations, their connection to phenomena on the Sun and to solar-wind structures, are of primary interest in determining space-weather effects on Earth.

Since the 1970s many solar-wind remote-sensing observing tools have become available, for example: sensitive coronagraphs, both ground-based and space-borne; heliospheric white-light imagers; X-ray imaging telescopes; low-frequency radio telescopes providing interplanetary scintillation (IPS) data; and space-borne kilometric-wave radio receivers. Determining the global properties of CMEs/ICMEs or more stable structures such as stream/co-rotating interaction regions (SIRs/CIRs), their morphology, and their motion, requires that these structures are tracked over an extended period of time during their outward propagation from the Sun. Heliospheric remote-sensing observations are of fundamental importance since they provide data on the solar-wind properties beyond the near-Sun region and those inaccessible to *in-situ* measurements.

IPS observations have long been used to remotely sense small-scale (80 – 300 km) heliospheric density variations in the solar wind crossing the line of sight (LOS) to a point-like astronomical radio source (*e.g.* Hewish, Scott, and Wills, 1964; Ananthakrishnan, Coles, and Kaufman, 1980). IPS provides a remotely sensed determination of the solar wind LOS-integrated bulk-density variation and the outward motion of transient structures including CMEs (Hewish and Bravo, 1986; Tokumaru *et al.*, 2003; Jackson and Hick, 2004; Jones

[4] Naval Research Laboratory, 4555 Overlook Ave., Washington, DC 20375, USA

[5] RAL Space, Science & Technology Facilities Council – Rutherford Appleton Laboratory, Harwell Oxford, Didcot OX11 0QX, UK

[6] Solar-Terrestrial Environment Laboratory (STELab), Nagoya University, Furo-cho, Chikusa-ku, Nagoya 464-8601, Japan

et al., 2007; Bisi *et al.*, 2007; Manoharan, 2010; Tokumaru, 2013). IPS observations, when subdivided into various distance regimes, have enabled the determination of the background solar-wind speed with distance from the Sun (Kojima *et al.*, 2004), and provided information on the interactions taking place between the Sun and Earth (*e.g.* Iju, Tokumaru, and Fujiki, 2013a, 2013b, 2014). These observations also permit a determination of the solar origins of these transient structures and their global morphology.

At the University of California, San Diego (UCSD), a time-dependent three-dimensional (3D)-reconstruction technique using IPS observations has been developed over a number of years (*e.g.* Jackson *et al.*, 2003; Hick and Jackson, 2004; Jackson and Hick, 2004; Jackson *et al.*, 2011). This Computer-Assisted Tomography (CAT) technique employs heliospheric remote-sensing data obtained from a single observing location, *i.e.* from Earth, and allows solar-wind temporal variations to be mapped in three spatial dimensions over time to provide 3D-reconstructed density and velocity distributions of heliospheric structure over the whole inner heliosphere. Since 1999, UCSD has implemented a near real-time 3D-reconstruction analysis using the Solar-Terrestrial Environment Laboratory (STELab) Japan IPS data, when available, to determine heliospheric structures in as close to real time as possible. Before 2010, STELab data were generally only available from May to December each year. Since the end of 2010, near real-time scintillation level observations have been available year round from a new array constructed in Toyokawa (Tokumaru *et al.*, 2011). Since 2005, the Current Sheet Source Surface (CSSS) potential magnetic field model (Zhao and Hoeksema, 1995) has been incorporated into the UCSD tomography analysis (Dunn *et al.*, 2005; Jackson *et al.*, 2012) as an extension from the kinematic model. The resulting reconstructed heliospheric density, velocity, and vector magnetic fields (radial and tangential field) are available as standard from 15 solar radii ($R_\odot$) out to 3.0 AU and can be extracted at any selected location within the reconstruction volume or can be used to provide a planar or constant solar distance contour plot. Recent kinematic analyses have been run to 4.5 AU to map a 3D response out to the distance of the ESA *Rosetta* spacecraft. The kinematic modeling becomes less accurate at these large distances. Additionally, the IPS-driven ENLIL model (Odstrcil, 2003) has recently been operated to as far from the Sun as 5.0 AU as a prediction program for this same reason.

Significant attention has been paid to numerical magnetohydrodynamic (MHD) modeling of CMEs/ICMEs and other heliospheric structures. A common approach used in global 3D-MHD simulations that provide time-dependent plasma distributions throughout the heliosphere is to divide the computational domain into two regimes: one near the origin of these features in the solar corona, and another that governs their propagation into the interplanetary space (*e.g.* Riley, Linker, and Mikić, 2001; Odstrcil and Pizzo, 2002; Odstrcil *et al.*, 2002a, 2003, 2008; Odstrcil, 2003; Riley, Mikic, and Linker, 2003; Odstrcil, Riley, and Zhao, 2004; Wu *et al.*, 2007; Riley *et al.*, 2011; Wu *et al.*, 2011, 2012; Liou *et al.*, 2014; also see a review: Lugaz and Roussev, 2011). A few attempts have also been made to simulate these two aspects simultaneously (*e.g.* Usmanov and Dryer, 1995; Wu *et al.*, 1999; Groth *et al.*, 2000; Feng *et al.*, 2010, 2011). From a space-weather perspective, it is important to study the propagation and evolution of solar events as they interact with one other and with the ambient solar wind, especially because of their possible geoeffective consequences. However, when simulating the propagation of these events, there is a complex chain of various dynamic phenomena that occurs simultaneously on different spatial and temporal scales. Moreover, knowledge of appropriate time-dependent conditions near the Sun is generally insufficient to directly drive numerical models, and thus various approximations must be used to provide inputs to CME modeling. These assumptions and lack of knowledge impede incorporating realistic solar-wind conditions into the modeling technique, and hence hinder the development of the 3D-MHD numerical simulations and the better physics provided by these analyses.

The use of iteratively fit kinematic modeling employing IPS and *Solar Mass Ejection Imager* (SMEI: Eyles *et al.*, 2003; Jackson *et al.*, 2004) observations to drive the 3D-MHD ENLIL model (Odstrcil, 2003) was first attempted in 2005 (Odstrcil *et al.*, 2005). At that time, only the IPS-derived velocity boundaries were used; densities were obtained from the SMEI Thomson-scattering brightness (Bisi *et al.*, 2008). However, this motivated UCSD to generate global solar-wind boundaries including magnetic field from the 3D-reconstruction of IPS remote-sensing data in a more general fashion (Yu *et al.*, 2012) to both drive and explore more thoroughly the differences in various 3D-MHD models. The present article continues this line of investigation, using IPS data to obtain both density and velocity, and for the first time it uses the modeled velocity to propagate the magnetic field in MHD models. Here, also for the first time, the results from two IPS-driven 3D-MHD models, ENLIL and H3D-MHD (Wu *et al.*, 2007) are compared with each other and with the IPS 3D reconstructions for the same interval in order to explore their differences using IPS results. Section 2 in this article describes our 3D-reconstruction technique for fitting STELab IPS velocity and scintillation-level data and the analysis that we use to provide extrapolated magnetic field in the heliosphere. An introduction to the 3D-MHD models developed for these analyses is also given in this section. We present sample determinations of the global solar-wind boundaries for input to 3D-MHD models from recent IPS data in Section 3. In Section 4 one sample period is explored using both the UCSD 3D reconstruction and 3D-MHD forward-modeling driven by the IPS-derived boundaries in order to better understand the detailed physical differences between model techniques. A discussion and summary are given in Section 5.

2. Heliospheric Remote-Sensing Analyses and Modeling

The information about the solar wind provided by IPS has been studied over many decades (*e.g.* Hewish, Scott, and Wills, 1964; Houminer, 1971; Ananthakrishnan, Coles, and Kaufman, 1980; Kojima and Kakinuma, 1987; Behannon, Burlaga, and Hewish, 1991; Kojima *et al.*, 1998; Jackson and Hick, 2004; Bisi *et al.*, 2007; Manoharan, 2010; Jackson *et al.*, 2010a, 2013; Mejia-Ambriz *et al.*, 2010, 2015). IPS is caused by the presence of density inhomogeneities in the solar wind, which disturb the signal from point-like radio sources. These produce intensity variations that, when projected onto Earth's surface, make a pattern that travels away from the Sun with the solar-wind speed. The correlation of this pattern between different radio sites allows a determination of the solar-wind outflow speed. The "normalized scintillation level" (g-level) of an IPS radio source signal relative to a nominal average value allows a determination of the solar-wind density. A greater variation in g-level amplitude generally means a higher plasma density along the LOS. The analysis of data from IPS radio arrays shows that heliospheric structures can be classified as either co-rotating or detached from the Sun (*e.g.* Behannon, Burlaga, and Hewish, 1991). The STELab IPS analysis is currently the primary source for UCSD velocity and density measurements; this also gives information about the *kinetic energy content* of the inner heliospheric solar-wind *bulk flow*.

2.1. UCSD Iterative Kinematic 3D-Reconstruction

The UCSD 3D-reconstruction technique using IPS data, developed since the early 1990s, provides a way to precisely determine heliospheric structure and to forecast CME and co-rotating structure arrival at Earth. Jackson *et al.* (1998) and Kojima *et al.* (1998) were the first to describe the methodology used in the 3D reconstructions; a recent review of the technique and its background has been given by Jackson *et al.* (2011). Jackson, Buffington, and Hick (2001) and Jackson, Hick, and Buffington (2003) first published the results of the time-dependent 3D-reconstruction IPS analyses. Details of the mathematical treatment of this technique were given by Hick and Jackson (2004) and Jackson *et al.* (2008). In addition to its use with STELab data, the time-dependent reconstruction analysis has been applied to IPS data from the *Ootacamund Radio Telescope* (ORT, or Ooty) in India (Bisi *et al.*, 2009b) as well as a small amount of data from the *European Incoherent SCAter* (EISCAT: Bisi *et al.*, 2007, 2010) radar. The Ooty data allow about twice-better angular and temporal resolution (*e.g.* Manoharan, 2010) in 3D. Recently, the reconstructions have been further refined to yield even more accurate densities and velocities in predictive and retrospective analyses by incorporating available *in-situ* data from spacecraft monitors near Earth (Jackson *et al.*, 2010a, 2013). The inclusion helps stabilize the global result and establishes a column of Sun-to-Earth density and velocity reflecting the *in-situ* values of these parameters. This inclusion changes the overall reconstructed solar-wind structure a only little, but yields a significantly better prediction of the variation of these *in-situ* parameters (relative to the last available values) in the near real-time analyses.

The 3D-reconstruction technique of STELab IPS data has also been used to predict the arrival of heliospheric structures in real time at the inner planets (Bisi *et al.*, 2009a; Jackson *et al.*, 2012, 2013), and now additionally at the two *Solar-TErrestrial RElations Observatory* (STEREO: Kaiser *et al.*, 2008) spacecraft. Since 2011 the analyses to incorporate available *in-situ* measurements near Earth of velocity and density into the real-time prediction have been in place at UCSD. Spatial and temporal resolutions from the 3D-reconstruction technique are limited by the current low-resolution IPS observational coverage and signal-to-noise ratio of each radio source observed. A STELab IPS time-dependent 3D reconstruction has a resolution of $20° \times 20°$ in latitude and longitude, and with steps of 0.1 AU in radial distance. The temporal cadence used here (usually one day for STELab data) is shorter than a solar rotation. The reconstruction volumes are smoothed with a set of Gaussian filters and extend from a 15 $R_\odot$ inner boundary out to ≈ 3 AU, with a one-day cadence. The larger STELab IPS radio array that began year-round scintillation-level observations in 2010 removed the restriction of using the STELab system for only a portion of the year.

The 3D reconstruction basically proceeds by least-squares fitting a purely kinematic heliospheric solar-wind model to the IPS LOS signal assuming radial outflow and enforcing conservation of mass and mass flux (Jackson *et al.*, 1998). LOS weighting is commensurate with the theoretical IPS weight function for weak scattering (Young, 1971). The LOS segment 3D weights and solar-wind parameters are projected back in space and time to a solar-wind inner boundary (sometimes also called the "source surface") that is usually set at 15 $R_\odot$. If the 3D solar-wind model does not match the overall observations, the inner boundary values are iteratively adjusted to minimize the differences between modeled and observed g-level and velocity. Inner-boundary Carrington maps of velocity and density are smoothed at each iteration using a 2D Gaussian spatial and temporal filter. Locations in the model that are unaffected by this iterative procedure (and thus undetermined) usually remain unfilled in the final result. Extensive study of this process has shown that the final iterated values are insensitive to the starting values on the source surface, and that the bulk of the convergence occurs within one or two iterations (Jackson *et al.*, 1998, 2008, 2010b).

The magnetic-field directions of transient heliospheric structures are important in determining how an interaction with planetary magnetic fields will proceed. If the heliospheric structure contains a southward interplanetary magnetic-field component (B_z negative), its field can couple with the magnetic field at Earth's magnetopause and trigger geomagnetic storms (Burlaga, Behannon, and Klein, 1987). In addition, solar energetic particles (SEPs), which account for some of the most damaging radiation hazards to high-flying aircraft and astronauts, are confined by the magnetic fields connecting the Sun with Earth. The CSSS magnetic-field model incorporated into the UCSD 3D-reconstruction analysis provides an accurate radial magnetic field projected from photospheric magnetic-field data (Dunn *et al.*, 2005; Jackson *et al.*, 2012); these data are updated as frequently as once a day at the IPS inner source surface. Since the CSSS model provides only radial magnetic fields and their variation at the source surface, the UCSD analysis extrapolates outward this heliospheric component of the radial field; the tangential magnetic-field component is provided by the rotation of the source surface below any specific location within the 3D volume and the velocity of the outward-flowing solar wind. Although these radial- and tangential-field components match *in-situ* measurements in Radial Tangential and Normal (RTN) coordinates fairly well over the long term, they do not include possible shorter-term transient features from such phenomena as CMEs (Dunn *et al.*, 2005). Because the field is radial at the 3D-reconstructed kinematic inner boundary, the usual CSSS analysis cannot provide an RTN normal component. In a recent article, however, Jackson *et al.* (2015) have shown that closed-loop propagation using the CSSS model can provide a significant portion of this normal-field component. We assume that 3D-reconstructed velocity is imposed on the magnetic fields that are "frozen-in" to the outward-expanding solar-wind plasma, and thus the radial IPS source surface field is determined and placed into the volumetric data only after the final kinematic model iteration.

2.2. ENLIL

The ENLIL (name of the Sumerian god of wind) 3D-MHD time-dependent heliospheric model, available at the Community Coordinate Modeling Center (CCMC), is based on an ideal 3D-MHD description, with two additional continuity equations used for tracking the injected CME material and the interplanetary magnetic-field polarity (Odstrcil and Pizzo, 1999). ENLIL (*e.g.* Odstrcil *et al.*, 2002b, 2004; Odstrcil, 2003; Odstrcil, Riley, and Zhao, 2004) was designed to easily incorporate various analytic, empirical, and numerical models (Odstrcil *et al.*, 2008). It distinguishes between the coronal and heliospheric regions with an interface located in the supercritical flow region. For ENLIL heliospheric computations, boundary conditions at the base of the computational grid are usually provided separately from photospheric magnetic-field observations interpreted in terms of velocity, and with an approximated value of temperature to provide density; the 3D-MHD model then extrapolates these and magnetic-field parameters outward. ENLIL has been long used to study the background solar wind and transient disturbances in the inner- and mid-heliosphere using velocity boundary conditions available from the Wang–Sheeley–Arge (WSA) model (Arge and Pizzo, 2000). ENLIL has also used inputs from the code Magnetohydrodynamics Around a Sphere (MAS: Mikic and Linker, 1994) for coronal modeling in place of WSA. The CME cone model (*e.g.* Zhao, Plunkett, and Liu, 2002) is often input on top of this background at 21.5 $R_\odot$ to drive CMEs. Here we replace the boundary conditions of both background solar wind and transient structures with inner boundary conditions obtained from the UCSD 3D-reconstruction technique incorporating IPS observations and available *in-situ* data (hereafter referred to as IPS-derived boundary) at 21.5 $R_\odot$.

2.3. H3D-MHD

The hybrid code H3D-MHD, also known as HAFv.2+3D-MHD (Wu *et al.*, 2007, 2011, and references therein), combines a 3D kinematic model, the code Hakamada–Akasofu–Fry, version 2 (HAFv.2), and a fully 3D time-dependent, single-fluid, ideal MHD simulation code. This hybrid code was originally designed to study the relationship between ICMEs at 1 AU and their solar sources, as well as to identify the possible origins of shock formation due to CME and CME/CIR or CME/CME interactions. Initially, the solar-wind velocity and radial interplanetary magnetic field are derived from daily solar photospheric magnetograms out to 2.5 $R_\odot$ by a potential field model such as WSA (Arge and Pizzo, 2000). The code HAFv.2 uses a modified kinematic approach to simulate the solar-wind conditions from 2.5 $R_\odot$ out to 18 $R_\odot$, which are then used as input for the 3D-MHD code to calculate the evolution of solar-wind plasma and interplanetary magnetic field beyond this distance. When simulating a solar event, a dynamic disturbance, mimicking the transient heliospheric structure, is delivered to this quiescent non-uniform background to model the evolution and interplanetary propagation of the ICME and/or shock structure. As with ENLIL, the H3D-MHD heliospheric code has been designed to be forward-modeled outward from an IPS-derived boundary that can be located from 18 $R_\odot$ to 40 $R_\odot$.

3. IPS-Derived Global Solar Wind Boundary

The UCSD 3D-reconstructed heliospheric density, velocity, and vector magnetic fields are available, as standard, from 15 $R_\odot$ out to 3.0 AU and can be extracted at any distance in between to provide inner boundary inputs to drive 3D-MHD forward modeling. The extracted 2D synoptic maps (IPS-derived boundaries) can be made available in many different coordinate frames, such as Inertial Heliographic coordinate (IHG) or RTN. In this article we present the latitude and longitude distribution of these parameters in Sun-centered Heliographic coordinates (HEEQ: Heliocentric Earth Equatorial, the Sun–Earth line is always located at 0° longitude), the normal coordinate system used for several 3D-MHD modeling efforts including H3D-MHD and ENLIL.

Figure 1 shows the STELab IPS-derived density, velocity, radial, and tangential magnetic field boundary conditions at 15 UT on 24 September 2011, when a CME sequence of interest first appears in the IPS reconstructions. For use as a continuous boundary for 3D-MHD modeling, the IPS 3D-reconstruction is interpolated to a fixed solar distance; additionally, the IPS global values are interpolated to a spatial and temporal resolution corresponding to that of the appropriate model. Here we extract these to provide the parameters for ENLIL, at 0.1 AU (21.5 $R_\odot$), this being the usual inner source surface distance used by this model. The spatial resolution of these boundary conditions is 4° in both latitude and longitude and presented at a six-hour cadence to ENLIL.

Similarly, Figure 2 shows these same quantities, but here extracted at 40 $R_\odot$ for input to the H3D-MHD model (Wu *et al.*, 2011), again at 15 UT on 24 September 2011. The spatial resolution provided at this boundary is 5° in both latitude and longitude and presented to the model with a one-hour cadence.

Figures 1a and 2a show many regions of high and low density spread over a wide range of longitudes. These coexist with patches of high- and low-velocity structure in Figures 1b and 2b. Generally, higher-speed/lower-density regions are present near the poles and lower-speed/higher-density regions are present near the heliographic Equator. For these figures and in the files given to the 3D-MHD modelers, an r^{-2} correction (applied to the density and

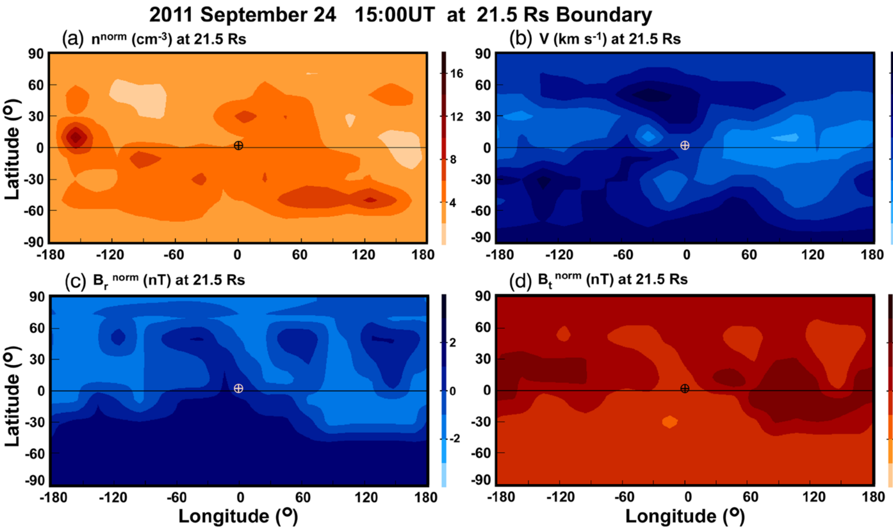

Figure 1 Global solar-wind boundaries of (a) density, (b) velocity, (c) radial, and (d) tangential magnetic field at 15 UT on 24 September 2011. These synoptic maps of solar wind parameters in HEEQ latitude and longitude coordinates are extracted at 21.5 $R_\odot$ from 3D tomographic analysis. The projected Earth location at 0° longitude and 7°N latitude is marked (⊕) on these synoptic maps.

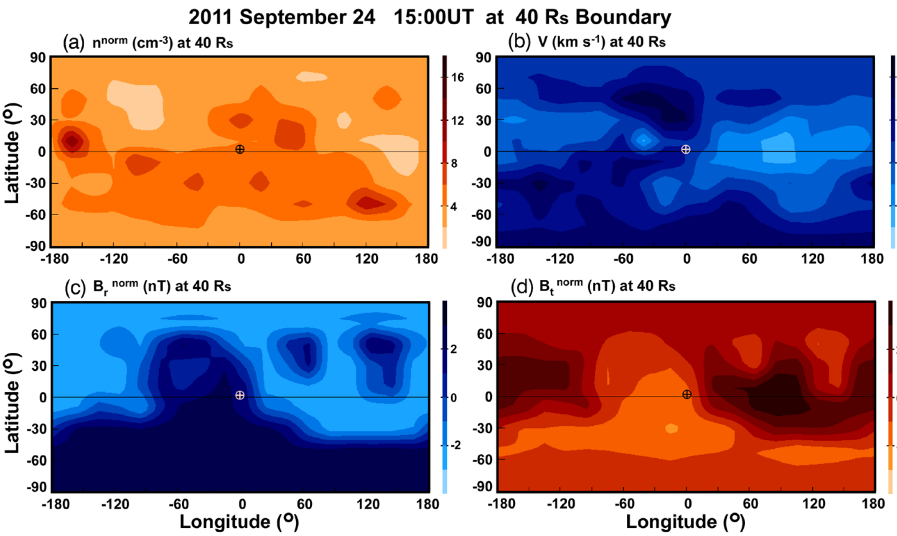

Figure 2 Global solar-wind boundaries of (a) density, (b) velocity, (c) radial, and (d) tangential magnetic field at 15 UT on 24 September 2011. These synoptic maps of solar wind parameters in HEEQ latitude and longitude are extracted at 40 $R_\odot$ from 3D tomographic analysis. The projected Earth is marked (⊕) on these synoptic maps.

normalized to 1 AU) maintains approximately the same scaling of features as they move outward from the Sun. The radial and tangential magnetic fields are also scaled with an r^{-2} and r^{-1} fall-off, respectively, relative to their values at 1 AU.

4. IPS-Derived 3D-MHD Boundary Results

The IPS-derived global 3D-reconstruction analysis is an iterative fit to IPS data as described in Section 2.1. This analysis also incorporates *in-situ* velocities and densities observed at Earth to provide a more accurate global boundary. Comparisons with velocity and density at Earth, especially results from the UCSD 3D-reconstruction analysis, are expected to be excellent, as detailed by Jackson *et al.* (2010a, 2013). Analyses using the IPS-derived boundary-driven 3D-MHD models should also best match *in-situ* values at Earth, but unlike the 3D-reconstruction results, these are forward-modeled from the given IPS-derived inner boundary instead of being iteratively fit to IPS observations and *in-situ* measurements.

4.1. Model Comparisons from a 35-Day Interval

Figure 3 shows density and velocity results from the UCSD kinematic 3D-reconstruction analysis and the forward-modeled 3D-MHD simulations, both compared with *Wind in-situ* measurements. The UCSD time-dependent analysis uses STELab IPS data from two Carrington rotations (CR2114 and CR2115) and incorporates the *Wind in-situ* density and velocity observations. The left-most panels show the long-term variations over 35 days for the density (top three panels) for the UCSD IPS analysis and the analysis made with ENLIL and H3D-MHD (dashed lines), and similarly for the velocity (bottom three panels). In each panel, the one-day averaged *Wind* observations are shown as solid lines. The right-hand panels of each pair show the Pearson "R" correlation coefficient between the IPS, ENLIL, and H3D-MHD results and the corresponding *Wind* values over this 35-day interval. This comparison shows how well the modeled analysis agrees with *in-situ* measurements. In this type of analysis, a perfect correlation of data provides a straight line of comparison points. Furthermore, a one-to-one correlation going through the origin with a slope of 1.0 shows agreement in magnitude of the two time series.

As expected, the UCSD kinematic model reproduces the *in-situ* record extremely well both in terms of the value of R (R is >0.9 for both velocity and density) and magnitude (shown by the slope of the line) at these resolutions (which are commensurate with the current STELab IPS 3D-reconstruction analysis). On the other hand, although the velocity from the 3D-MHD models has a fairly high correlation with the *in-situ* measurements, the H3D-MHD velocity is on average about 40 $\mathrm{km\,s^{-1}}$ higher than the kinematic modeling velocity. The ENLIL velocity also matches *in-situ* measurements in R and slope well. However, in these analyses the IPS-derived velocity was reduced by 75 $\mathrm{km\,s^{-1}}$ everywhere before it was used as an ENLIL inner boundary to provide the agreement with *in-situ* measurements. These differences are discussed in detail in Section 5. The IPS-driven 3D-MHD models reproduce the *in-situ* densities well, but there is a noticeable spike (particularly in the ENLIL results) at the arrival time of the shock/CME. Larger excursions from the *in-situ* values in both 3D-MHD models are also found in the low-density and low-velocity regions near their peak values.

A shorter timescale (seven-day) comparison around the shock arrival time (12 UT on 26 September, see Section 4.2 for detail) is presented in the right-hand pairs of panels in Figure 3 in a similar format. The IPS 3D-reconstruction analysis and the 3D-MHD modeling results are presented in their native (low) resolutions in all of the figures. However, while the *in-situ* measurements presented in the left panels in Figure 3 have a one-day boxcar average imposed, those in the right panels have only a six-hour boxcar average imposed instead. This allows easily locating features in the *in-situ* record that are more sharply defined, such as the shock response. When this is done, the IPS iteratively derived modeling density loses

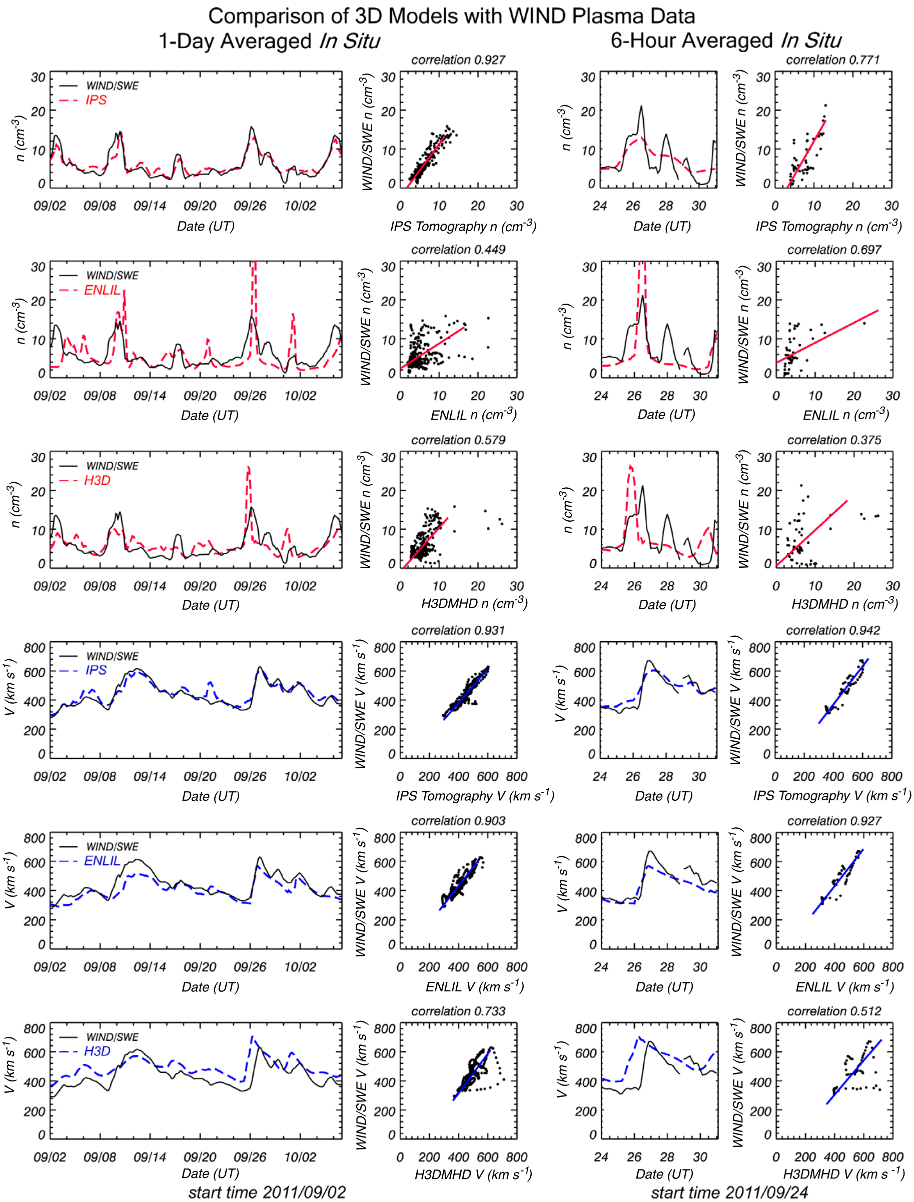

Figure 3 Comparisons of the STELab IPS time-dependent UCSD kinematic solution and the IPS-driven 3D-MHD simulations (ENLIL and H3D-MHD) with *Wind in-situ* observations. The top three rows show the density from the UCSD IPS analysis, IPS-driven ENLIL, and IPS-driven H3D-MHD. The bottom three rows show the velocity from the UCSD IPS analysis, IPS-driven ENLIL, and IPS-driven H3D-MHD.

some of its high correlation with the *in-situ* measurements as a result of its intrinsic low resolution and poor capability of exploring shock processes. The magnitude of the density spike shown in the IPS-driven H3D-MHD model matches the primary shock response seen in the *in-situ* record better, but it is displaced in time somewhat earlier than the actual arrival

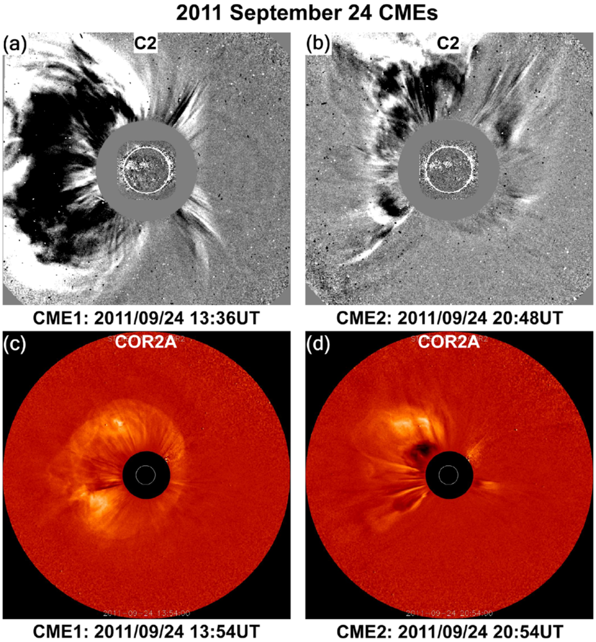

Figure 4 The CMEs observed as halo events in SOHO/LASCO-C2 difference images and in the STEREO/COR2A background-subtracted coronagraphs. (a) CME1 observed by C2 at 13:36 UT. (b) CME2 observed by C2 at 20:48 UT. (c) CME1 observed by COR2A at 13:54 UT. (d) CME2 observed by COR2A at 20:54 UT.

time. This reduces the correlation coefficients for both density and velocity comparisons with the *in-situ* measurements. On the other hand, although the shock magnitude in the IPS-driven ENLIL model is significantly greater than the actually observed magnitude, the shock arrival time is well simulated. This and the reduction of the IPS-derived velocity boundary effectively improve the agreement of ENLIL results with *in-situ* measurements. Therefore, both density and velocity from the ENLIL modeling have a higher R, and the slope matches the *in-situ* measurements better than do the results from H3D-MHD modeling.

We now examine this event sequence over the time interval depicted in the right panels to explore the reasons for these differences.

4.2. A Specific CME Example, 24 September 2011

This interval is of special interest because two halo CMEs were observed on 24 September 2011 by the *Large Angle and Spectrometric COronagraph* (LASCO: Brueckner *et al.*, 1995) C2, and the first was an extremely energetic event. The CME was not announced as being extremely energetic by forecasters until a couple of days later. Although the speed estimated for the first halo CME in LASCO was reported to be over 2000 km s^{-1} (Schenk, [Soho-halo-alert] SOHO/LASCO HALO CME 110924ab), the response at Earth did not appear within the short time interval expected to result from such a speed.

The first CME (CME1), which first appeared at 12:48 UT in the LASCO-C2 field of view, was listed as having a speed of 1915 km s^{-1} in the SOHO/LASCO CME Coordinated Data Analysis Workshops (CDAW) catalog (cdaw.gsfc.nasa.gov/CME_list/UNIVERSAL/2011_09/univ2011_09.html). The second CME (CME2), first observed by LASCO-C2 at 19:36 UT, was listed as having a speed of 972 km s^{-1} and originated from the same source region on the Sun. Figure 4 shows example images of these two halo CMEs from the perspective of both the LASCO-C2 coronagraphs (difference images) and STEREO/COR2A

Figure 5 HI-1A difference images (left panels) of the two CMEs (observed as halos by the LASCO-C2 and -C3 coronagraphs) as they move outward from the Sun along the Sun–Earth line (marked as a horizontal line in the HI images). The right panels show the time this feature is measured by various instruments at different heights. (a) CME1. (b) CME2.

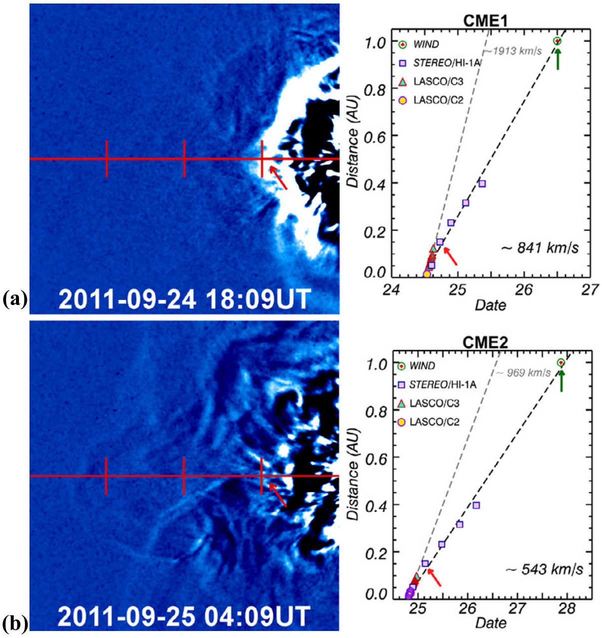

coronagraphs (background-subtracted images). At this time the STEREO spacecraft were situated at HEEQ longitudes of 97° East (ST-Behind, −97°), and 104° West (ST-Ahead, +104°) of Earth. From these vantage points, the STEREO/COR2 coronagraphs (Howard *et al.*, 2008) and the STEREO/*Heliospheric Imagers* (HI-1: Eyles *et al.*, 2009) could easily view both CMEs as they traveled outward toward the Earth. CME1 propagated directly toward Earth at such a fast initial speed that, with no deceleration, it would have reached Earth and caused a severe geomagnetic storm within one day (Figure 4a and 4c). CME2 moved at a slower initial speed and was directed higher above the solar equatorial plane (Figure 4b and 4d).

HI-1A and HI-1B data are now well calibrated and thus can be easily inter-compared in terms of brightness (Eyles *et al.*, 2007, 2009; Harrison *et al.*, 2008; Brown, Bewsher, and Eyles, 2009; Bewsher, Brown, and Eyles, 2012). Figure 5 shows the HI-1A images of the CMEs. The brightness of CME1 as seen by HI-1B is about the same as it is in HI-1A, indicating that it is located fairly symmetrically with respect to the Sun–Earth line. CME2, however, is brighter in HI-1A, thus indicating that it is closer to STEREO-A and thus its main bulk lies west of the Sun–Earth line. CME2 fades away more quickly in HI-1B images than in HI-1A images. In both LASCO-C2 and in the COR2 coronagraphs there is significant evidence for a considerable amount of CME2 material directed both North and South of the ecliptic plane during this halo event, but the longitudinal ecliptic extent of this CME is unclear. These observations indicate that the bulk of CME2 mass is directed more westward along the Ecliptic as seen from Earth than is that of CME1.

We approximate the height profile of these CMEs along the Sun–Earth line by assuming that their main response contribution, along any LOS, comes from the point of closest approach of the line of sight to the Sun and that the CME can be represented as a spherical shell projected to the Sun–Earth line. Superposed on the HI-1A images in Figure 5, left-hand panels, are red-vertical line segments that indicate (right to left) elongations of 10°, 15°, and 20° from the Sun in the ecliptic plane (the latter is marked by a horizontal line). The aforementioned assumptions are used to translate the elongation profiles of the two CMEs into the height–time diagrams in the ecliptic plane, shown in the right-hand panels of Figure 5. The red arrows in the HI-1A image correspond to the red arrows in the height–time plots; these features of CME1 and CME2 are tracked along the ecliptic plane. The heights of the CMEs in the C2 and C3 fields of view measured to the solar Northeast as listed in the SOHO/LASCO CDAW CME Catalog and the CME arrival time at Earth (*in-situ* observation, green arrow) are also plotted.

The speed of CME1 is shown to have decreased dramatically in the HI-1 field of view compared with its speed observed by LASCO-C2. This explains its "late" arrival at Earth. Its motion is tracked at about 800 $\mathrm{km\,s^{-1}}$ along the Sun–Earth line, arriving at Earth at around 12 UT on 26 September. This is manifest by shock arrival followed by magnetic field, velocity, density, and temperature enhancements detected *in situ* at 1 AU (see Richardson, 2013). The shock associated with CME1 corresponds to the highest density peak on 26 September (see Figure 3). A strong-to-severe ($K_{\mathrm{p}} = 8$) or intense ($D_{\mathrm{st}} < -100$ nT) geomagnetic storm (Tsurutani and Gonzalez, 1997) caused by a CME1 impact was reported by the NOAA Space Weather Prediction Center. The NASA Goddard Space Weather Lab also reported a strong compression of Earth's magnetosphere (www.nasa.gov/mission_pages/sunearth/news/News092511-ar1302.html). The speed of CME2 along the Sun–Earth line derived from the height–time profile is much slower than its initial speed of 972 $\mathrm{km\,s^{-1}}$ estimated using the LASCO imagery (confirmed by arrival time at Earth).

Figure 6 shows examples of the ecliptic cuts of both density and velocity from the 3D-MHD models and, for comparison, the IPS 3D-reconstruction analysis. Figure 6 presents the density in the left panels and the velocity in the right panels generally at the time CME1 has arrived at Earth. Figure 6a shows the ecliptic cuts of the ENLIL model driven by the IPS-derived boundary at 21.5 $\mathrm{R}_{\odot}$. Similar ecliptic cuts are shown for the H3D-MHD model driven by IPS boundaries at 40 $\mathrm{R}_{\odot}$ in Figure 6b. Figure 6c shows an ecliptic cut of the IPS 3D-reconstruction model. The density plots show that CME1 curves towards STEREO-A and has a high-density impact at Earth; however, CME2 (especially from the IPS reconstruction) propagates roughly about 20° west of the Sun–Earth line and just misses Earth. Followed by the arrival of CME1's high-density front, a high-speed structure reaches Earth and lasts for several days.

5. Discussion and Summary

The propagation direction, potential Earth arrival time, and solar origin of rapidly varying transient heliospheric structures (like CMEs) are important especially from a space-weather perspective. Velocity is an extremely important parameter, but the velocity of the daily rapidly varying transient *background* solar-wind structure outside CMEs beyond the near-Sun region currently cannot be measured remotely in any other way than by IPS observations. CMEs, included in any IPS line-of-sight observations, are inseparable from this background in the UCSD analysis except as an enhancement of the general background. CME speeds can also be estimated from the passage of their high-density fronts through the fields of view of coronagraphs or heliospheric imagers. Moreover, a Type-II radio burst can also provide a proxy for CME shock velocity (*e.g.* Sun *et al.*, 2008; Schmidt and Cairns, 2014), and these estimated velocities are used as CME velocities input to H3D-MHD by the use of the Hakamada–Akasofu–Fry (HAF) kinematic CME propagation model (Fry *et al.*, 2002).

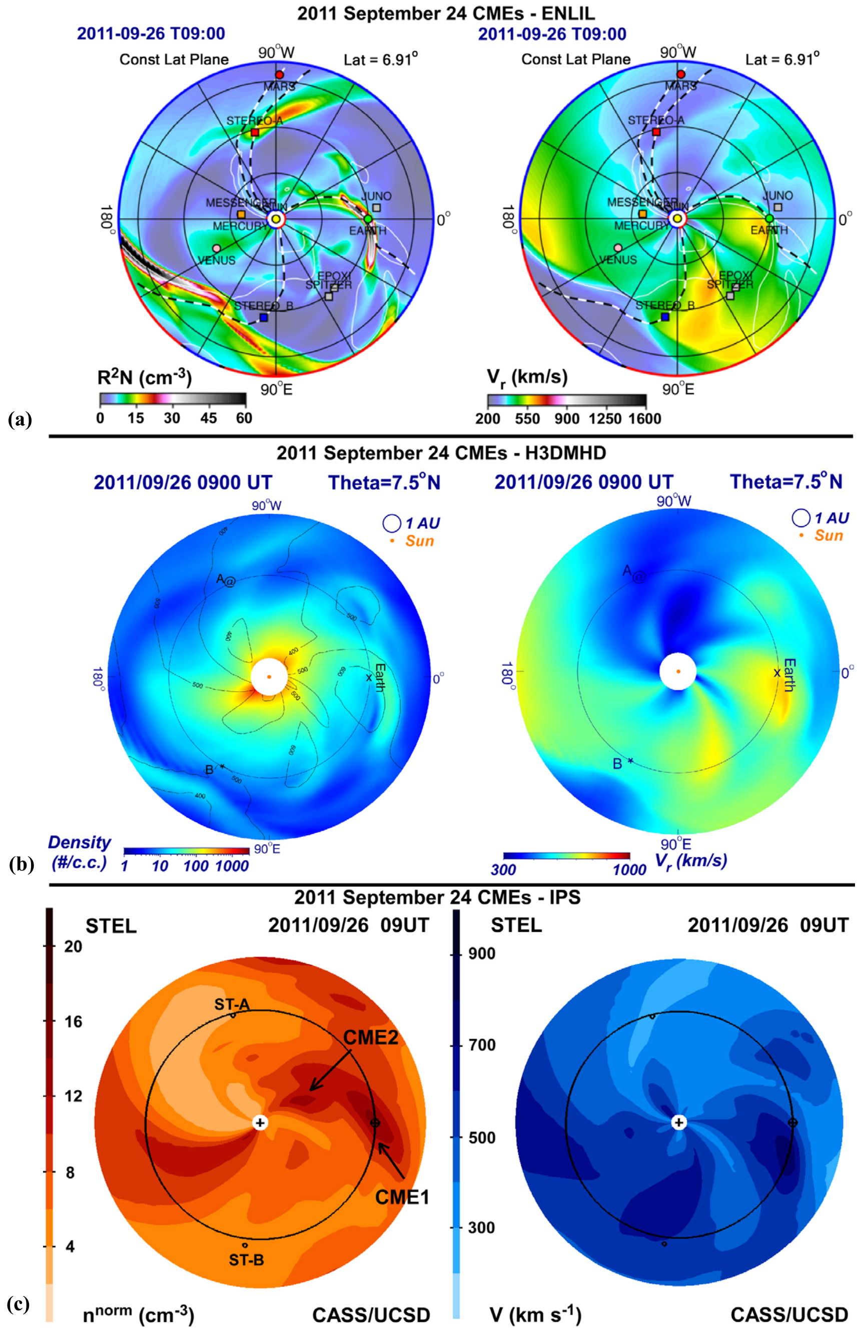

Figure 6 Planar cut plots of the CME propagation. The location of the Earth on its circular orbit is shown to right in each plot. (a) Density and velocity ecliptic cuts from ENLIL driven by IPS boundaries at 21.5 $R_\odot$. The dashed lines in the analysis show the solar stream connections to various objects within the heliosphere (Earth, STEREO-A and -B). (b) H3D-MHD model driven by IPS boundaries at 40 $R_\odot$. The lines on the density plot trace various speed contours for the same time presented in the speed plot to the right. (c) IPS 3D-reconstructed ecliptic cuts provided at the same time for comparison.

Because of insufficient knowledge of appropriate time-dependent conditions near the Sun, heliospheric 3D-MHD modeling generally relies on the use of magnetic-field observations on the solar surface to provide estimates of plasma parameters (velocity, density, and temperature). In the usual ENLIL analysis, the background solar-wind speed is provided by the outward extrapolation and the divergence of photospheric magnetic fields to obtain an *ad-hoc* relationship between velocity and magnetic-field quantities (Wang and Sheeley, 1990). The density of the background solar wind is usually provided by assuming a constant mass flux outward flow once the speed has been determined. Thus, the speed and density are indirectly inferred quantities, and they may not be applicable everywhere on the Sun. Fast transient events (*i.e.* CMEs) are injected into this background with densities and velocities that are likewise difficult to determine in 3D, and are generally either i) best-guess approximations to the 3D source of energy that ejects plasma from the Sun such as loop current activation, or ii) 3D fits to the coronagraph data to provide the outward motion of fast-moving transient structures. Thus, the 3D-MHD models could well use the IPS 3D-reconstruction analyses to determine *both* the slow background solar wind and the fast transient components, especially when other means of determining the input source surface parameters are unavailable.

In both the IPS 3D-reconstruction analysis and the 3D-MHD modeling efforts, solar photospheric magnetograms are usually extrapolated outward, using a potential-field source surface and current-sheet model to obtain background 3D magnetic-field distributions near the Sun that can be further extrapolated outward into the heliosphere. Direct measurements of the rapidly varying transient CME magnetic field are essentially absent except in special well studied cases. Once background fields are determined, the 3D-MHD modeling should provide relatively good handling (relative to the kinematic modeling) of interactions between fast and slow speed structures, as fast transient structures move outward into the heliosphere.

The UCSD 3D-reconstructions provide low spatial and temporal resolution estimates of densities and velocities of all LOS heliospheric structures including the 3D density and velocity structure of CMEs. However, the physics behind the kinematic modeling is inadequate when used in the low corona (where magnetic fields dominate), in regions very distant from the Sun, or when exploring shock processes that are not considered by the UCSD analysis. Numerical solar-wind models based on the MHD equations are currently the only self-consistent mathematical descriptions capable of bridging many AUs outward from near the Sun to well beyond Earth's orbit. Even though 3D-MHD models have successfully simulated many important space-plasma processes, the various assumptions on which 3D-MHD relies means that it too can only provide an approximation to actual plasma behavior. Thus, comparing the two different 3D-MHD modeling techniques, run using the same boundary conditions, with results of the kinematic modeling can be expected to yield valuable insights and maybe even some discoveries. Below, we provide examples that suggest a way to further refine both techniques.

Figures 1 and 2 show an example of IPS 3D-reconstructed boundary conditions for the two different 3D-MHD models explored in this analysis. The spatial resolution ($5^\circ \times 5^\circ$ for H3D-MHD, $4^\circ \times 4^\circ$ for ENLIL) is nearly the same and boundaries are presented from the same time. The UCSD 3D-reconstruction technique incorporates a purely kinematic solar-wind model that enforces conservation of mass and mass flux (Jackson *et al.*, 2008) at a $20^\circ \times 20^\circ$ resolution. Because this technique provides similar boundaries at 40 $R_\odot$ (for H3D-MHD) and 21.5 $R_\odot$ (for ENLIL), both 3D-MHD analyses should give similar results, since the primary drivers of these models in the inner heliosphere are the speed and density of the plasma.

The speeds from the IPS-driven 3D-MHD models generally average about 40 $\mathrm{km\,s^{-1}}$ higher at 1 AU than those from the IPS kinematic analysis. The IPS-driven Multi-Scale FLUid-Kinetic Simulation Suite (MS-FLUKSS) 3D-MHD model (Kim *et al.*, 2014) shows this as well. This is generally attributed to the adiabatic expansion of the solar wind inherent in the 3D-MHD modeling. The value of gamma [γ], the ratio of specific heats, and the temperature or thermal-pressure difference between the inner boundary and larger distances from the Sun, imparts an outward expansion of the solar wind, which increases its speed at 1 AU beyond what would be expected from the simple momentum and mass-flux conservation, which is assumed in the UCSD kinematic model. Studies of the interactions between interplanetary shocks in the inner heliosphere using 1.5D- (Wu, Wu, and Dryer, 2004) and 3D- (Wu *et al.*, 2011) MHD simulations show no significant γ-dependence. Wu *et al.* thus concluded that $\gamma = 5/3$, the value for a monatomic gas with three degrees of freedom, is the best choice for the solar wind at 1 AU, and hence this value is used in the H3D-MHD model. In the ENLIL model, γ is also chosen to be $5/3$. However, the temperature at the inner boundary is not well known, and the value of γ for the different solar wind constituents (protons, helium ions, electrons) for both H3D-MHD and ENLIL are assumed to be the same. An acceleration of the solar wind as it moves outward through the heliosphere has some credence from the IPS observations of Kojima *et al.* (2004), who subdivided the IPS analyses into two different solar distances. They found a slightly higher speed farther from the Sun during Carrington Rotations 1909 – 1913 in 1996. However, this increase in speed between 0.2 and 0.6 AU was found to be only 20 – 40 $\mathrm{km\,s^{-1}}$ and only then for the high-speed wind. To achieve a better velocity match with *in-situ* values at Earth, we carried out a test run by implementing a 10 % reduction in the IPS-derived velocity boundary used to drive the H3D-MHD model. Although the timing of the velocity peaks corresponds better with the *Wind* values when this is done, there are larger excursions at other times, particularly from 10 – 14 September 2011 and for the peak speeds on 27 September (similar to those from ENLIL shown in Figure 3). An *ad-hoc* run with the IPS velocity boundary modified using the formula $V_{\mathrm{MHD\_40\,R_\odot}} = (V_{\mathrm{IPS\_40\,R_\odot}} - 100) \times 1.2$ over the whole simulation enhances the peaks and troughs and gives a better overall fit to the *in-situ* observations. However, the arrival times of the peaks are then not as well determined, and thus the correlation R with *in-situ* measurements does not improve. A similar scaling is also used in the IPS-driven ENLIL modeling to better match *in-situ* velocity values to match the overall R and slope of the correlations (Odstrcil *et al.*, 2014). If the ENLIL code did not have boundary speeds reduced by 75 $\mathrm{km\,s^{-1}}$ into which the higher-speed features were inserted, the higher-speed regions would have arrived too early and the correlation R would have decreased. Thus, many esoteric physical mechanisms not yet incorporated into the IPS-driven 3D-MHD models may need to be included to improve their accuracy.

The observed decrease in the velocity excursions in the 3D-MHD model results could be caused by smoothing present in the kinematic modeling that progressively damps the IPS response with solar distance, or by interpolation of the IPS boundaries when converted from the UCSD RTN 3D co-rotational coordinate system to the intrinsic 3D-MHD coordinate system. However, there is no obvious decrease in the velocity excursions, even though we experimented with IPS-derived boundary resolutions of as great as 1.0° in the MS-FLUKSS where this effect is even greater (see Kim *et al.*, 2014). Thus, because the boundaries are similar for all models, we believe this arises from the way in which each 3D-MHD model operates. We suspect that either the solar-wind temperature (assumed to be different in each model) or the assumption of non-radial flow (present in the 3D-MHD models but not incorporated in the UCSD kinematic model) could account for the "fill-in" effects near peaks and troughs in the *in-situ* velocity record.

The physical mechanisms that decrease the variations of density and velocity with height in the inner heliosphere are only poorly understood as yet. The most egregious differences between the results of the 3D-MHD models and the *in-situ* record arise from the models' inability to show shock peaks with excursions that are as small as those measured *in situ* (see top panels of Figure 3). In the 3D-MHD results, these density peaks are caused by the high velocities in the solar wind imposed on the inner boundary generally from fast CMEs such as CME1.

There is strong evidence of a shock associated with CME1 that arrives at 1 AU at ≈ 12 UT on 26 September having an associated increase in density, velocity, temperature, and magnetic field observed by *Wind* near Earth (Richardson, 2013). The density and velocity synoptic maps at the inner boundary (Figures 1 and 2) show a relatively dense high-speed structure close to the projected Earth location near the center of the map. The fitted speed (841 $\mathrm{km\,s^{-1}}$) from the height–time profile of this event, derived from its elongation variation in the HI-1A images (Figure 5a), agrees well with the *in-situ Wind* speed. This speed is not overestimated by the boundary conditions shown for the same event at the projected Earth location in Figures 1 and 2. One explanation for the discrepancy between the peak shock density from the 3D-MHD modeling and the *in-situ* measurements is that the temperatures in either the background wind or especially above the CME ejecta are higher than elsewhere. This has the effect of reducing the peak shock density responses (Odstrcil *et al.*, 2014).

Another phenomenon that could generally provide a less enhanced velocity response and a dampened shock-density response is an interaction between the solar wind and dust in the solar wind by mass-loading and particle-grain collisions. This could transfer kinetic energy from solar wind to grains, or to ions originating at grains (*e.g.* Jones *et al.*, 2002, 2003). A charged-dust effect between solar wind and dust trails, interplanetary field enhancements (IFEs), has recently been observed (Lai, Wei, and Russell, 2013) and simulated (*e.g.* Jia *et al.*, 2012); this effect can cause retardation of solar-wind speed and a possible decrease in the enhancement of solar wind density. The magnetic field enhancement in IFEs removes momentum from the solar wind and transfers it to charged nanoscale dust particles. These dust particles are generally thought to be released in interplanetary collisions of bodies whose sizes range from tens to hundreds of meters (Lai, Wei, and Russell, 2013). As a result, the solar-wind plasma is slowed down due to the continuous momentum loss of the IFEs, and this momentum can lift the dust outward in the solar gravity well.

In summary, the UCSD tomographic 3D-reconstruction fits a purely kinematic heliospheric solar-wind model to IPS LOS signal and *in-situ* measurements at Earth, assuming radial outflow and enforcing conservation of mass and mass flux. This provides 3D time-dependent estimates of the background solar wind and embedded CME structures. The 3D-MHD models are time-dependent, single-fluid, ideal MHD simulations with additional equations for tracking a best-guess of injected CME material. In these MHD models we use IPS-derived inner-boundary conditions for density, velocity, and vector magnetic field. In comparison with the IPS kinematic analysis, we find that the MHD models show an average speed higher by 40 $\mathrm{km\,s^{-1}}$, show larger excursions in velocity and density, and an overestimated shock density. These discrepancies could be caused by adiabatic expansion of the solar wind and non-radial flow that are not present in the UCSD kinematic model. Physical mechanisms not incorporated in either the MHD models or kinematic model, such as solar-wind mass-loading by dust and particle-grain collision effects, might also be a factor.

Improving the quality of IPS-derived boundary data sets is one way to reduce the differences between the model results and the observations. The UCSD 3D-reconstruction analysis currently based on STELab IPS data and *in-situ* density and velocity can also be employed to use the density determined from the brightness of electron Thomson-scattered sunlight, such as those from SMEI as in Jackson *et al.* (2008). Contemporary systems that can be used in these analyses include STEREO HI-1 and HI-2 observations, together with STEREO and other deep-space probes *in-situ* density and velocity observations. An ultimate goal of this work is to improve the UCSD 3D-reconstruction technique by replacing the kinematic model by a 3D-MHD model – an inclusive "3D-MHD 3D-reconstruction" iterative analysis. Looking even further ahead, a 3D-reconstruction analysis that can incorporate all of the inputs currently available to MHD modeling as well as the IPS analyses with appropriate weighting relative to each incorporated input will be the ultimate we can envision for investigating and predicting the location of heliospheric structures as they move outward from the Sun.

Acknowledgements H.-S. Yu, B.V. Jackson, P.P. Hick, and A. Buffington were supported at UCSD by NSF grants AGS-1053766, and AGS-1358399, and by AFOSR grant FA9550-11-1-0324. Work of C.-C. Wu was supported by the ONR 6.1 program. The authors wish to acknowledge and thank the group at STELab, Nagoya University (those not included in the author list: M. Kojima, K. Fujiki, and students) for their continued support, and for making IPS data sets available under the auspices of a joint collaborative agreement between the Center for Astrophysics and Space Sciences at UCSD and STELab, Nagoya University. We wish to thank Kevin Schenk and the LASCO coronagraph group for the CME images taken using the C2 coronagraph, and the STEREO/SECCHI group for making available their COR2 images. We also thank the UKSSDC (UK solar system data centre) for providing the HI data.

Disclosure of Potential Conflicts of Interest The authors declare that they have no conflicts of interest.

References

Ananthakrishnan, S., Coles, W.A., Kaufman, J.J.: 1980, *J. Geophys. Res.* **85**, 6025. DOI.
Arge, C.N., Pizzo, V.J.: 2000, *J. Geophys. Res.* **105**, 10465. DOI.
Behannon, K.W., Burlaga, L.F., Hewish, A.: 1991, *J. Geophys. Res.* **96**, 21213. DOI.
Bewsher, D., Brown, D.S., Eyles, C.J.: 2012, *Solar Phys.* **276**, 491. DOI.
Bisi, M.M., Jackson, B.V., Fallows, R.A., Breen, A.R., Hick, P.P., Wannberg, G., Thomasson, P., Jordan, C., Dorrian, G.D.: 2007, *Proc. SPIE* **6689**, 1. DOI.
Bisi, M.M., Jackson, B.V., Hick, P.P., Buffington, A., Odstrcil, D., Clover, J.M.: 2008, *J. Geophys. Res.* **113**, A00A11. DOI.
Bisi, M.M., Jackson, B.V., Buffington, A., Clover, J.M., Hick, P.P., Tokumaru, M.: 2009a, *Solar Phys.* **256**, 201. DOI.
Bisi, M.M., Jackson, B.V., Clover, J.M., Manoharan, P.K., Tokumaru, M., Hick, P.P., Buffington, A.: 2009b, *Ann. Geophys.* **27**, 4479. DOI.
Bisi, M.M., Jackson, B.V., Breen, A.R., Dorrian, G.D., Fallows, R.A., Clover, J.M., Hick, P.P.: 2010, *Solar Phys.* **265**, 233. DOI.
Brown, D.S., Bewsher, D., Eyles, C.J.: 2009, *Solar Phys.* **254**, 185. DOI.
Brueckner, G.E., Howard, R.A., Koomen, M.J., Korendyke, C.M., Michels, D.J., Moses, J.D., Socker, D.G., Dere, K.P., Lamy, P.L., Llebaria, A., Bout, M.V., Schwenn, R., Simnett, G.M., Bedford, D.K., Eyles, C.J.: 1995, *Solar Phys.* **162**, 357. DOI.
Burlaga, L.F., Behannon, K.W., Klein, L.W.: 1987, *J. Geophys. Res.* **92**, 5725. DOI.
Dunn, T., Jackson, B.V., Hick, P.P., Buffington, A., Zhao, X.P.: 2005, *Solar Phys.* **227**, 339. DOI.
Eyles, C.J., Simnett, G.M., Cooke, M.P., Jackson, B.V., Buffington, A., Hick, P.P., Waltham, N.R., King, J.M., Anderson, P.A., Holladay, P.E.: 2003, *Solar Phys.* **217**, 319. DOI.
Eyles, C., Davis, C., Harrison, R., Waltham, N., Halain, J.-P., Mazy, E., Defise, J.-M., Howard, R., Moses, D., Newmark, J., Plunkett, S.: 2007, *Proc. SPIE* **6689**, 5. DOI.
Eyles, C.J., Harrison, R.A., Davis, C.J., Waltham, N.R., Shaughnessy, B.M., Mapson-Menard, H.C.A., Bewsher, D., Crothers, S.R., Davies, J.A., Simnett, G.M., Howard, R.A., Moses, J.D., Newmark, J.S., Socker, D.G., Halain, J.-P., Defise, J.-M., Mazy, E., Rochus, P.: 2009, *Solar Phys.* **254**, 387. DOI.
Feng, X., Yang, L., Xiang, C., Wu, S.T., Zhou, Y., Zhong, D.: 2010, *Astrophys. J.* **723**, 300. DOI.
Feng, X., Zhang, S., Xiang, C., Yang, L., Jiang, C., Wu, S.T.: 2011, *Astrophys. J.* **734**, 50. DOI.
Fry, C.D., Sun, W., Deehr, C., Dryer, M., Smith, Z., Akasofu, S.-I.: 2002, In: Wang, H., Xu, R. (eds.) *Proc. COSPAR Colloq.* **14**, Pergamon, Boston, 401.

Gosling, J.T., McComas, D.J., Phillips, J.L., Bame, S.J.: 1991, *J. Geophys. Res.* **96**, 7831. DOI.
Groth, C.P.T., De Zeeuw, D.L., Gombosi, T.I., Powell, K.G.: 2000, *J. Geophys. Res.* **105**, 25053. DOI.
Harrison, R.A., Davis, C.J., Eyles, C.J., Bewsher, D., Crothers, S.R., Davies, J.A., Howard, R.A., Moses, D.J., Socker, D.G., Newmark, J.S., Halain, J.-P., Defise, J.-M., Mazy, E., Rochus, P., Webb, D.F., Simnett, G.M.: 2008, *Solar Phys.* **247**, 171. DOI.
Hewish, A., Bravo, S.: 1986, *Solar Phys.* **106**, 185. DOI.
Hewish, A., Scott, P.F., Wills, D.: 1964, *Nature* **203**, 1214. DOI.
Hick, P.P., Jackson, B.V.: 2004, *Proc. SPIE* **5171**, 287. DOI.
Houminer, Z.: 1971, *Nat. Phys. Sci.* **231**, 165. DOI.
Howard, R.A., Moses, J.D., Vourlidas, A., Newmark, J.S., Socker, D.G., Plunkett, S.P., Korendyke, C.M., Cook, J.W., Hurley, A., Davila, J.M., Thompson, W.T., St Cyr, O.C., Mentzell, E., Mehalick, K., Lemen, J.R., Wuelser, J.P., Duncan, D.W., Tarbell, T.D., Wolfson, C.J., Moore, A., Harrison, R.A., Waltham, N.R., Lang, J., Davis, C.J., Eyles, C.J., Mapson-Menard, H., Simnett, G.M., Halain, J.P., Defise, J.M., Mazy, E., Rochus, P., Mercier, R., Ravet, M.F., Delmotte, F., Auchere, F., Delaboudiniere, J.P., Bothmer, V., Deutsch, W., Wang, D., Rich, N., Cooper, S., Stephens, V., Maahs, G., Baugh, R., McMullin, D., Carter, T.: 2008, *Space Sci. Rev.* **136**, 67. DOI.
Iju, T., Tokumaru, M., Fujiki, K.: 2013a, In: Borovsky, J., Bruno, R., Cirtain, J., Cranmer, S., Elliott, H., Giacalone, J., Gonzalez, W., Li, G., Marsch, E., Moebius, E., Pogorelov, N., Spann, J., Verkhoglyadova, O., Zank, G.P. (eds.) *AIP Conf. Proc.* **1539**, 183.
Iju, T., Tokumaru, M., Fujiki, K.: 2013b, *Solar Phys.* **288**, 331. DOI.
Iju, T., Tokumaru, M., Fujiki, K.: 2014, *Solar Phys.* **289**, 2157. DOI.
Jackson, B.V., Hick, P.P.: 2004, In: Gary, D.E., Keller, C.U. (eds.) *Solar and Space Weather Radiophysics Current Status and Future Developments, ASSL* **314**, Springer, Berlin, 355.
Jackson, B.V., Buffington, A., Hick, P.P.: 2001, *Solar Encounter: The First Solar Orbiter Workshop* **SP-493**, ESA, Noordwijk, 251.
Jackson, B.V., Hick, P.P., Buffington, A.: 2003, *Proc. SPIE* **4853**, 23.
Jackson, B.V., Hick, P.L., Kojima, M., Yokobe, A.: 1998, *J. Geophys. Res.* **103**, 12049. DOI.
Jackson, B.V., Hick, P.P., Buffington, A., Kojima, M., Tokumaru, M., Fujiki, K., Ohmi, T., Yamashita, M.: 2003, In: Velli, M., Bruno, R., Malara, F. (eds.) *AIP Conf. Proc.* **679**, 75.
Jackson, B.V., Buffington, A., Hick, P.P., Altrock, R.C., Figueroa, S., Holladay, P.E., Johnston, J.C., Kahler, S.W., Mozer, J.B., Price, S., Radick, R.R., Sagalyn, R., Sinclair, D., Simnett, G.M., Eyles, C.J., Cooke, M.P., Tappin, S.J., Kuchar, T., Mizuno, D., Webb, D.F., Anderson, P.A., Keil, S.L., Gold, R.E., Waltham, N.R.: 2004, *Solar Phys.* **225**, 177. DOI.
Jackson, B.V., Bisi, M.M., Hick, P.P., Buffington, A., Clover, J.M., Sun, W.: 2008, *J. Geophys. Res.* **113**, A00A15. DOI.
Jackson, B.V., Hick, P.P., Bisi, M.M., Clover, J.M., Buffington, A.: 2010a, *Solar Phys.* **265**, 245. DOI.
Jackson, B.V., Buffington, A., Hick, P.P., Bisi, M.M., Clover, J.M.: 2010b, *Solar Phys.* **265**, 257. DOI.
Jackson, B.V., Hick, P.P., Buffington, A., Bisi, M.M., Clover, J.M., Tokumaru, M., Kojima, M., Fujiki, K.: 2011, *J. Atmos. Solar-Terr. Phys.* **73**, 1214. DOI.
Jackson, B.V., Hick, P.P., Buffington, A., Clover, J.M., Tokumaru, M.: 2012, *Adv. Geosci.* **30**, 93. DOI.
Jackson, B.V., Clover, J.M., Hick, P.P., Buffington, A., Bisi, M.M., Tokumaru, M.: 2013, *Solar Phys.* **285**, 151. DOI.
Jackson, B.V., Hick, P.P., Buffington, A., Yu, H.-S., Bisi, M.M., Tokumaru, M., Zhao, X.: 2015, *Astrophys. J. lett.* **803**, 1. DOI.
Jia, Y.-D., Ma, Y.J., Russell, C.T., Lai, H.R., Toth, G., Gombosi, T.I.: 2012, *Icarus* **218**, 895. DOI.
Jones, G.H., Lucek, E.A., Balogh, A., MacDowall, R.J., McComas, D.J., Smith, E.J.: 2002, *J. Geophys. Res.* **107**, 1054. DOI.
Jones, G.H., Balogh, A., McComas, D.J., MacDowall, R.J.: 2003, *Icarus* **166**, 297. DOI.
Jones, R.A., Breen, A.R., Fallows, R.A., Canals, A., Bisi, M.M., Lawrence, G.: 2007, *J. Geophys. Res.* **112**, 8107. DOI.
Kaiser, M.L., Kucera, T.A., Davila, J.M., St Cyr, O.C., Guhathakurta, M., Christian, E.: 2008, *Space Sci. Rev.* **136**, 5. DOI.
Kim, T.K., Pogorelov, N.V., Borovikov, S.N., Jackson, B.V., Yu, H.-S., Tokumaru, M.: 2014, *J. Geophys. Res.* **119**, 7981. DOI.
Kojima, M., Kakinuma, T.: 1987, *J. Geophys. Res.* **92**, 7269. DOI.
Kojima, M., Tokumaru, M., Watanabe, H., Yokobe, A., Asai, K., Jackson, B.V., Hick, P.L.: 1998, *J. Geophys. Res.* **103**, 1981. DOI.
Kojima, M., Breen, A.R., Fujiki, K., Hayashi, K., Ohmi, T., Tokumaru, M.: 2004, *J. Geophys. Res.* **109**, 4103. DOI.
Lai, H.R., Wei, H.Y., Russell, C.T.: 2013, In: Borovsky, J., Bruno, R., Cirtain, J., Cranmer, S., Elliott, H., Giacalone, J., Gonzalez, W., Li, G., Marsch, E., Moebius, E., Pogorelov, N., Spann, J., Verkhoglyadova, O., Zank, G.P. (eds.) *AIP Conf. Proc.* **1539**, 402.

Liou, K., Wu, C.-C., Dryer, M., Wu, S.-T., Rich, N., Plunkett, S., Simpson, L., Fry, C.D., Schenk, K.: 2014, *J. Atmos. Solar-Terr. Phys.* **121**, 32. DOI.
Lugaz, N., Roussev, I.I.: 2011, *J. Atmos. Solar-Terr. Phys.* **73**, 1187. DOI.
Manoharan, P.K.: 2010, *Solar Phys.* **265**, 137. DOI.
Mejia-Ambriz, J.C., Villanueva-Hernandez, P., Gonzalez-Esparza, J.A., Aguilar-Rodriguez, E., Jeyakumar, S.: 2010, *Solar Phys.* **265**, 309. DOI.
Mejia-Ambriz, J.C., Jackson, B.V., Gonzalez-Esparza, J.A., Buffington, A., Tokumaru, M., Aguilar-Rodriguez, E.: 2015, *Solar Phys.* (accepted).
Mikic, Z., Linker, J.A.: 1994, *Astrophys. J.* **430**, 898. DOI.
Odstrcil, D.: 2003, *Adv. Space Res.* **32**, 497. DOI.
Odstrcil, D., Pizzo, V.J.: 1999, *J. Geophys. Res.* **104**, 483. DOI.
Odstrcil, D., Pizzo, V.J.: 2002, In: Sawaya-Lacoste, H. (ed.) *SOLSPA 2001, The Second Solar Cycle and Space Weather Euroconference* **SP-477**, ESA, Noordwijk, 281.
Odstrcil, D., Riley, P., Zhao, X.P.: 2004, *J. Geophys. Res.* **109**, 2116. DOI.
Odstrcil, D., Linker, J.A., Lionello, R., Mikic, Z., Riley, P., Pizzo, V.J., Luhmann, J.G.: 2002a, In: Wilson, A. (ed.) *Solar Variability: From Core to Outer Frontiers* **SP-506** ESA, Noordwijk, 95.
Odstrcil, D., Linker, J.A., Lionello, R., Mikic, Z., Riley, P., Pizzo, V.J., Luhmann, J.G.: 2002b, *J. Geophys. Res.* **107**, 1493. DOI.
Odstrcil, D., Riley, P., Linker, J.A., Lionello, R., Mikic, Z., Pizzo, V.J.: 2003, In: Wilson, A. (ed.) *Solar Variability as an Input to the Earth's Environment* **SP-535**, ESA, Noordwijk, 541.
Odstrcil, D., Pizzo, V.J., Linker, J.A., Riley, P., Lionello, R., Mikic, Z.: 2004, *J. Atmos. Solar-Terr. Phys.* **66**, 1311. DOI.
Odstrcil, D., Pizzo, V.J., Arge, C.N., Bisi, M.M., Hick, P.P., Jackson, B.V., Ledvina, S.A., Luhmann, J.G., Linker, J.A., Mikic, Z., Riley, P.: 2008, In: Pogorelov, N.V., Audit, E., Zank, G.P. (eds.) *ASP Conf. Proc.* **CS-385**, Astron. Soc. Pac., San Francisco, 167.
Odstrcil, D., Jackson, B., Yu, H.-S., Hong, S., Kim, J.: 2014, *AOGS Meeting* **ST23**, Sapporo, Hokkaido, A010.
Odstrcil, D., Pizzo, V.J., Arge, C.N., Jackson, B.V., Hick, P.P.: 2005, *SPIE* (title and presentation only, see: ftp://cass185.ucsd.edu/Presentations/2005_SPIE).
Richardson, I.G.: 2013, *J. Space Weather Space Clim.* **3**, 08. DOI.
Riley, P., Linker, J.A., Mikić, Z.: 2001, *J. Geophys. Res.* **106**, 15889. DOI.
Riley, P., Mikic, Z., Linker, J.A.: 2003, *Ann. Geophys.* **21**, 1347. DOI.
Riley, P., Lionello, R., Linker, J.A., Mikic, Z., Luhmann, J., Wijaya, J.: 2011, *Solar Phys.* **274**, 361. DOI.
Schmidt, J.M., Cairns, I.H.: 2014, *J. Geophys. Res.* **119**, 69. DOI.
Sun, W., Deehr, C.S., Dryer, M., Fry, C.D., Smith, Z.K., Akasofu, S.-I.: 2008, *Space Weather* **6**, 3006. DOI.
Tokumaru, M.: 2013, *Proc. Japan Acad. Ser. B, Phys. Biol. Sci.* **89**, 67. DOI.
Tokumaru, M., Kojima, M., Fujiki, K., Yamashita, M., Yokobe, A.: 2003, *J. Geophys. Res.* **108**, 1220. DOI.
Tokumaru, M., Kojima, M., Fujiki, K., Maruyama, K., Maruyama, Y., Ito, H., Iju, T.: 2011, *Radio Sci.* **46**, RS0F02. DOI.
Tsurutani, B.T., Gonzalez, W.D.: 1997, *Geoph. Monog. Ser.* **98**, AGU, Washington, 77.
Usmanov, A.V., Dryer, M.: 1995, *Solar Phys.* **159**, 347. DOI.
Wang, Y.-M., Sheeley, N.R. Jr.: 1990, *Astrophys. J.* **355**, 726. DOI.
Wu, C.-C., Wu, S.T., Dryer, M.: 2004, *Solar Phys.* **223**, 259. DOI.
Wu, C.-C., Fry, C.D., Wu, S.T., Dryer, M., Liou, K.: 2007, *J. Geophys. Res.* **112**, A09104. DOI.
Wu, C.-C., Dryer, M., Wu, S.T., Wood, B.E., Fry, C.D., Liou, K., Plunkett, S.: 2011, *J. Geophys. Res.* **116**, A12103. DOI.
Wu, C.-C., Liou, K., Wu, S.T., Dryer, M., Fry, C.D., Plunkett, S.: 2012. In: Li, G., Pogorelov, N., Zank, G., Heerikhuisen, J. (eds.) *AIP Conf. Proc.* **1436**, 285.
Wu, S.T., Guo, W.P., Michels, D.J., Burlaga, L.F.: 1999, *J. Geophys. Res.* **104**, 14789. DOI.
Young, A.T.: 1971, *Astrophys. J.* **168**, 543. DOI.
Yu, H.-S., Jackson, B.V., Hick, P.P., Buffington, A., Clover, J.M., Tokumaru, M.: 2012. In: Li, G., Zank, G.P., Ao, X., Verkhoglyadova, O., Adams, J.H., Hu, Q. (eds.) *AIP Conf. Proc.* **1500**, 147.
Zhao, X., Hoeksema, J.T.: 1995, *J. Geophys. Res.* **100**, 19. DOI.
Zhao, X.P., Plunkett, S.P., Liu, W.: 2002, *J. Geophys. Res.* **107**, 1223. DOI.